Accepted Manuscript

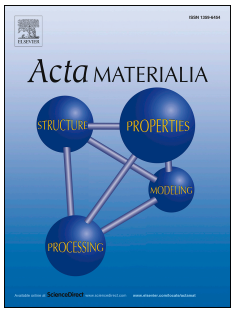

Half-Heusler phase formation and Ni atom distribution in M-Ni-Sn (M = Hf, Ti, Zr) systems

Matylda N. Guzik, Cristina Echevarria-Bonet, Marit D. Riktor, Patricia A. Carvalho, Anette E. Gunnæs, Magnus H. Sørby, Bjørn C. Hauback

PII: S1359-6454(18)30050-8

DOI: 10.1016/j.actamat.2018.01.019

Reference: AM 14313

To appear in: *Acta Materialia*

Received Date: 19 September 2017

Revised Date: 18 December 2017

Accepted Date: 19 January 2018

Please cite this article as: M.N. Guzik, C. Echevarria-Bonet, M.D. Riktor, P.A. Carvalho, A.E. Gunnæs, M.H. Sørby, B.C. Hauback, Half-Heusler phase formation and Ni atom distribution in M-Ni-Sn (M = Hf, Ti, Zr) systems, *Acta Materialia* (2018), doi: 10.1016/j.actamat.2018.01.019.

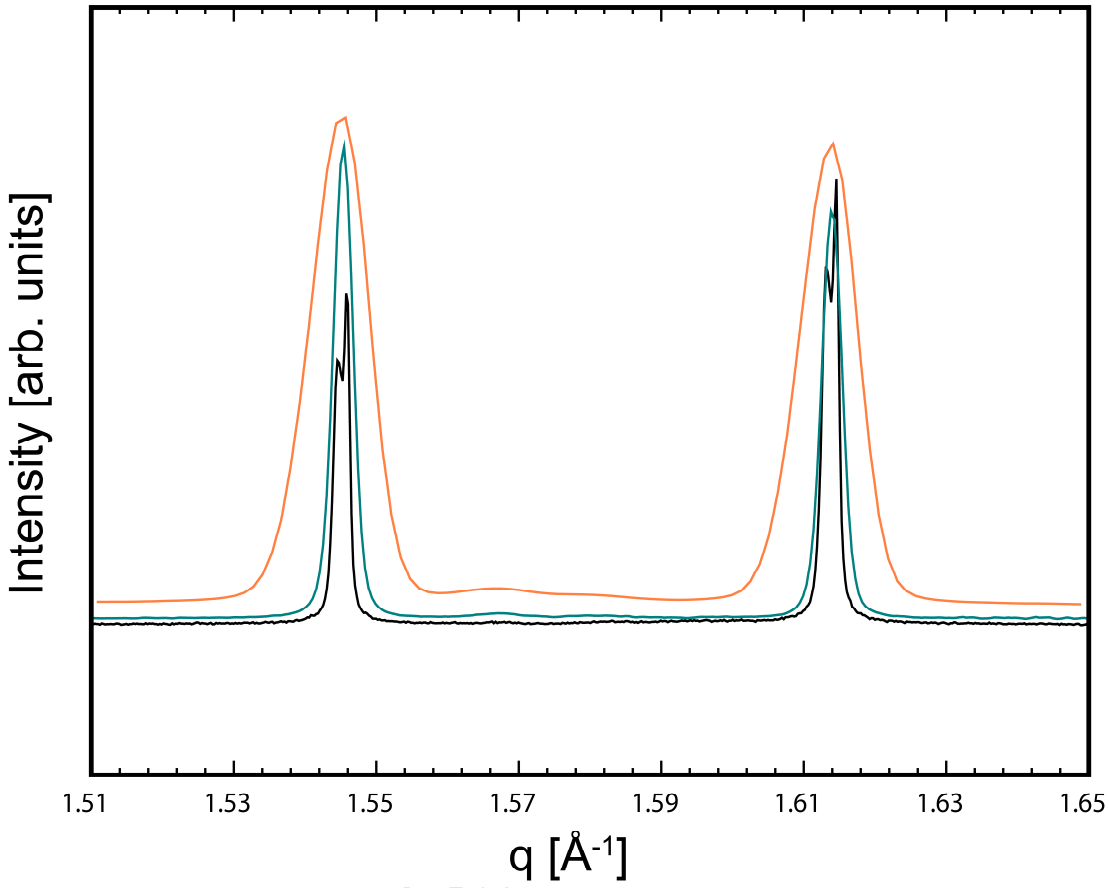

Half-Heusler Phase Formation and Ni Atom Distribution in M-Ni-Sn (M = Hf, Ti, Zr) systems

Matylda N. Guzik[1,2], Cristina Echevarria-Bonet[1], Marit D. Riktor[3], Patricia A. Carvalho[3], Anette E. Gunnæs[2], Magnus H. Sørby[1], Bjørn C. Hauback[1]

[1]Physics Department, Institute for Energy Technology, P.O. Box 40, N-2027 Kjeller, Norway

[2]Department of Physics, University of Oslo, Blindern, P.O. Box 1048, N-0316 Oslo, Norway

[3]SINTEF Materials and Chemistry, P.O. Box 124, N-0316 Oslo, Norway

Abstract High resolution synchrotron radiation powder X-ray diffraction (SR-PXD) and scanning transmission electron microscopy (STEM) have been employed for structural characterization of MNiSn, $M_{0.5}M'_{0.5}NiSn$ and $M_{0.5}M'_{0.25}M''_{0.25}NiSn$ (M, M', M'' = Hf, Ti, Zr) half-Heusler compounds, synthesized by arc melting and thermal annealing. Rietveld refinement results demonstrate that ternary Ti- and Hf-based compositions crystallize with only one half-Heulser phase, while two cubic phases are found in samples with nominal composition ZrNiSn. The performed analysis does not suggest obvious presence of excess Ni in any of the ternary compounds. Instead, it shows disordered distribution of the stoichiometric Ni atoms over *4c* and the normally vacant *4d* sites in ZrNiSn as well as formation of Ni vacancies at the *4c* site in $ZrNi_{0.98}Sn$.

Introduction

The appealing concept to recover waste heat by using thermoelectric generators has been explored theoretically and experimentally since the 50's [1-3], but has turned out to be challenging in practice. To make it possible, one needs to overcome both the limitation imposed by the Carnot efficiency of a device and a thermoelectric material itself. The effectiveness is characterized by the so-called "figure of merit", termed zT. It is defined by three parameters: the Seebeck coefficient, the electrical and the thermal conductivities, which are strongly correlated through the material electronic structure and thus difficult to optimize independently. Extensive efforts to identify the most promising groups of thermoelectric materials have recognized half-Heusler (HH) phases as potential candidates [4]. A family of compounds with composition MNiSn (M = Hf, Ti, Zr) has attracted a special attention. High thermoelectric performance, low toxicity, mechanical robustness and inexpensive constituents make them very attractive for technological applications. However, the characteristics of HH compounds include some challenges that must be addressed before they can be effectively implemented commercially. One of the main identified obstacles is the high thermal conductivity in HHs as compared to their alternatives [5, 6]. Various synthesis and processing methods, modifying compound chemistry and microstructure, have been pursued to tailor the properties of HH phases [5-7], but an approach that could sufficiently improve their thermoelectric behavior is still to be identified.

A good understanding of the crystal structure is a key point in optimization of the material thermoelectric performance [7-10] since the two are intrinsically linked. HH

compounds, with a general chemical formula *ABC* (*A*, *B* – transition metal atom, *C* – main group element), crystallize with a cubic symmetry (*F*-43*m*). Their crystal structure can be perceived as an interpenetration of four face-centered cubic lattices, of which one is vacant. Thus, for the studied MNiSn phases, four characteristic crystallographic sites can be distinguished: *4a* (0,0,0) occupied by M, *4c* (¼, ¼, ¼) occupied by Ni, *4b* (½, ½, ½) occupied by Sn and the additional unfilled tetrahedral *4d* site (¾, ¾, ¾). While many studies refer to thermoelectric properties of this family of compounds focusing on transport and conductivity aspects, there is a limited number of publications dedicated to its systematic structural characterization. Downie et al. investigated TiNiSn, and series of MNiSn (M = Hf, Ti, Zr) samples prepared by solid stated reaction using high-resolution powder neutron diffraction (PND) [11, 12]. For TiNiSn the study showed the presence of excess Ni (2%) in the HH crystal structure, distributed over the nominally vacant *4d* site, or a possible mixed occupancy of the *4a* and *4b* crystallographic positions (3%) by Ti/Sn. In the Sn-deficient sample a higher fraction of Ni was found to be disordered at the *4d* site (6%) or Ti/Sn inverse site occupancy up to 9% was suggested. Furthermore, they reported a stoichiometric composition for ternary Hf- and Zr-based compounds. Downie et al. also analyzed PND data of TiNiSn and $TiNiSn_{0.95}$ powders prepared by arc melting and thermal annealing [13]. In this case, a higher fraction of excess Ni was observed for the Sn-deficient composition than for the nominally stoichiometric TiNiSn (6 vs. 4%, respectively). In both compounds overstoichiometric Ni atoms occupied the *4d* site. In none of the structures a substantial mixed atomic occupancy of the *4a* and *4b* sites by Ti and Sn was observed. Regardless of the applied synthesis method, all obtained samples, except for TiNiSn prepared by solid state reaction, revealed a multiphase composition [11, 14]. The same

research group also reported on structural characterization of $M_{1-x}M'_xNiSn$ (M, M' = Hf, Ti, Zr; x = 0, 0.25, 0.5, 0.75, 1) compounds prepared by solid state reaction from elemental powder mixtures [12, 14]. While laboratory powder X-ray diffraction (PXD) data confirmed the formation of multiphase HH phases in all investigated pseudo-ternary compositions[14], the quantitative analysis of high resolution PND data additionally suggested the presence of overstoichiometric Ni in selected $Ti_{1-x}Zr_xNiSn$ and $Hf_{1-x}Ti_xNiSn$ phases [11]. In contrary to the previous PXD analysis, $Hf_{0.5}Zr_{0.5}NiSn$ crystallized as a single HH phase and it did not show any disorder of the Ni atom distribution. Downie et al. also performed systematic PND studies on series of $TiNi_{1+y}Sn$ (y = 0, 0.025, 0.05, 0.075, 0.1, 0.25, 0.5, 1) compounds [12], where the coexistence of a TiNiSn matrix and nanosegregated $TiNi_2Sn$ full-Heusler (FH) phase was observed. In this study, they pointed out the importance of the diffraction data quality for the reliable structural analysis of HH-FH compounds. Douglas et al. investigated TiNiSn and $TiNi_{1.15}Sn$ prepared by levitation induction melting and thermal annealing [15]. Results obtained by synchrotron radiation PXD (SR-PXD) and PND suggested the multiphase behavior of the nominally stoichiometric sample. Diffraction data for the Ni-rich composition also indicated presence of more than one HH phase. The best fit of the powder diffraction pattern was obtained by applying a structural model consisting of two TiNiSn HH phases, of which one was stoichiometric, while the second one accommodated excess Ni at the *4d* site (5% from PND data). These studies excluded a possible mixed occupancy of *4a* and/or *4b* sites by Ti and Sn. Xie et al. [16] and Miyazaki et al. [17] performed structural investigations of ZrNiSn synthesized by levitation/arc melting and spark plasma sintering. Densified, sintered pellets were measured by SR-PXD. Both studies confirmed the presence of disorderly distributed

overstoichiometric Ni in the crystal structure of the single HH phase. The analysis showed excess Ni atoms at the *4d* site and excluded inverse occupancy of *4a* and *4b* positions by Zr and Sn. The amount of extra Ni accounted for 5% and 9% in studies by Xie et al. and Miyazaki et al., respectively [16, 17]. Structural analysis with PXD and single crystal diffraction for the stoichiometric ZrNiSn and HfNiSn by Romaka et al. [18, 19] confirmed full occupancy of the *4c* site by Ni atoms and suggested its disordered distribution at the normally vacant tetrahedral site (9 and 13% of Ni for ZrNiSn; 11% of Ni for HfNiSn). Interestingly, they observed a mixed Zr/Ni and Hf/Ni occupancy with 1% of Ni at the *4a* site in both investigated compounds. Galazka et al. [20] performed Le Bail profile fitting of laboratory PXD data collected for $Ti_{0.33}Zr_{0.33}Hf_{0.33}NiSn$ prepared by arc meting and thermal annealing. The results showed formation of four structurally related phases with different unit cell parameters, of which one was indexed as FH phase and the remaining three as HH phases. The studied sample also contained small amount of impurity phases. Similar SR-PXD studies on a sample with a nominal composition $Ti_{0.5}Zr_{0.25}Hf_{0.25}NiSn$ were performed by Schwall and Balke [21], where they observed formation of only three HH phases. Analysis of unit cell parameters indicated crystallization of Ti- and Hf-rich compositions.

The studies performed so far clearly show that crystallization of HH compounds is strongly linked with the applied synthesis and processing techniques. PXD and PND data for the M-Ni-Sn ternary systems often reveal broadening and/or asymmetry of cubic phase reflections and thus suggest a presence of more than one HH phase. This cannot be easily discriminated due to either strong overlapping of Bragg peaks with the available resolution of the powder diffraction data or/and intrinsic sample properties related to a complex powder microstructure [5, 11, 13, 15]. The problem appears to be even more pronounced in

$M_{1-x}M'_xNiSn$ and $(MM')_{1-x}M''_xNiSn$ with a partial atomic substitution, for which formation of several HH phases is an intrinsic materials' property [11, 14, 20-22]. Even though PXD is the most common technique used for qualitative and quantitative analysis of MNiSn phases, not many users are sufficiently aware that the limited resolution of diffraction instruments can hinder correct identification of the formed phases and their structural and microstructural properties. To verify whether it is a sample- and/or measurement-related problem, a systematic analysis of HH sample series is necessary. In order to partly answer this question, we have investigated a family of HH compounds with the nominal compositions: MNiSn, $M_{0.5}M'_{0.5}NiSn$ and $M_{0.5}M'_{0.25}M''_{0.25}NiSn$ (M, M', M'' = Hf, Ti, Zr) by using medium- and high-resolution SR-PXD instruments. Our analysis is focused on identification of crystallizing phases and their structural characterization in view of the Ni atom distribution and shows the benefit of obtaining data with diffraction instruments optimized for high resolution measurements (i.e. equipped with point detectors and analyzer crystals) rather than a fast, multipurpose setup with a 2D area detector. The SR-PXD analysis is complemented and verified by the electron microscopy studies.

1. Materials and methods

Polycrystalline samples of HH compounds, with nominal compositions TiNiSn, HfNiSn, ZrNiSn, $Hf_{0.5}Zr_{0.5}NiSn$, $Hf_{0.5}Ti_{0.5}NiSn$, $Ti_{0.5}Zr_{0.5}NiSn$ and $Ti_{0.5}Hf_{0.25}Zr_{0.25}NiSn$, were prepared by standard metallurgical methods. Pieces/powders of elemental precursors (Ni, Sn, Zr – Goodfellow; Hf, Ti – Alpha Aesar, purity > 99.5%) were first arc melted in the desired stoichiometric ratios. To improve sample homogeneity the ingot was flipped over several times and remelted. Subsequently, the ingot was crushed to powder, sealed in

an evacuated quartz ampoule, annealed at 850 °C for one week and eventually water quenched. The choice of annealing time and temperature was optimized based on our and literature studies in order to ensure the highest concentration of the HH(s) and the lowest abundance of secondary phases in the sample [11-15, 17, 20, 21]. SR-PXD measurements of the heat-treated powders were carried out at ESRF, Grenoble (France). Data were collected at the ID22 beamline equipped with a high-resolution powder X-ray diffractometer (λ = 0.4000 Å, 2θ = 1- 66°, point detectors with analyzer crystals). Selected compositions were also measured with the multipurpose PILATUS@SNBL diffractometer with 2D area detector at the Swiss-Norwegian Beamline (the BM01 station, λ = 0.6973 Å), at ESRF. Data collection at BM01 was done with two different instrumental settings. The standard mode with a sample-to-detector distance of 146.4 mm allowed for measurements to higher 2θ values (cut off = 60°) but at expense of data resolution. The higher resolution mode, with a much larger sample-to-detector distance (646.4 mm) limited the 2θ measurement range to 24° but provided a significantly better data resolution. The powders were ground and loaded in sealed boron-glass capillaries, with 0.3 mm (ID22) or 0.5 mm (BM01) diameter, which were rotated during measurements to improve powder averaging. The collected data sets for the same sample with different instrumental setups are presented in Figure 1.

Data were analyzed by conventional Rietveld refinement using the Fullprof Suite program [23]. Depending on the compound, regular or Thomson-Cox-Hastings pseudo-Voigt peak shape function was used to model the diffraction profiles. The SR-PXD background was defined by interpolation of manually chosen points. For the identified HH phase(s), the following parameters were allowed to vary for each phase during the final

refinement cycles: a scale factor, up to seven profile parameters (Gaussian (U, V, W), Lorentzian (X, Y) and two asymmetry parameters), unit cell parameter, overall or individual displacement parameter(s), occupancy factor for *4b*, *4c* and *4d* sites in MNiSn, and *4a* instead of *4b* for pseudo-ternary $M_{0.5}M'_{0.5}NiSn$ and $M_{0.5}M'_{0.25}M''_{0.25}NiSn$. The data were corrected for X-ray absorption, which was calculated assuming a packing fraction of 0.5 in the capillaries.

The elemental analysis of all powders was carried out in a Hitachi tabletop microscope TM3030 equipped with the energy dispersive X-ray spectrometer (EDS) Quantax 70. Annular bright-field (ABF) and high-angle annular dark field (HAADF) scanning transmission electron microscopy (STEM) coupled to EDS was employed to characterize the local structural properties and chemical compositions of selected samples (TiNiSn, ZrNiSn, $Hf_{0.5}Zr_{0.5}NiSn$). This work was performed with a DCOR Cs probe-corrected FEI Titan G2 60-300 instrument, with 0.08 nm nominal spatial resolution when operated at 300 kV, equipped with a Bruker SuperX EDS system comprising four silicon drift detectors. TEM specimens were prepared by depositing droplets of sample powders suspended in isopropanol on Cu-grids with lacey carbon films. After drying, shielded plasma cleaning was performed for 90 seconds.

2. Results

2.1. High resolution synchrotron powder X-ray diffraction (SR-PXD)

The inability to resolve the Bragg peaks in the medium resolution laboratory/synchrotron data of our samples resulted in opposing conclusions and

questioned the reliability of the analysis. Thus, all results presented here are based on high-resolution SR-PXD data. Various structure models were tested for ternary MNiSn compositions. The results did not indicate M/Sn inversed site occupancy. For selected HH phases, a significant improvement of the data fit was achieved when partial occupation of Ni in the normally vacant *4d* site was included in the refinements. For all studied ternary systems, refinements were performed assuming a full occupancy of the *4a* atomic site by M atom(s). Due to the significant difference in electron numbers between Ti and Sn, a crystal structure model with the Sn site (*4b*) constrained to 100% was also tested for TiNiSn. No changes in refined parameters were observed except for the higher values of estimated standard deviations (ESDs), as compared to the model with Ti-constrained site occupancy. For $M_{0.5}M'_{0.5}NiSn$ and $M_{0.5}M'_{0.25}M''_{0.25}NiSn$ compositions, the convergence during refinements was not always reached when applying a structural model that accounted for the occupancy of the *4d* site. Thus for selected systems, this atomic position was omitted in the final refinements.

2.1.1. Ternary MNiSn phases

The diffraction data for the nominally stoichiometric TiNiSn show presence of three crystalline phases (Figure S1). In addition to the most abundant TiNiSn (98.6(3) wt.%), both $TiNi_2Sn$ FH phase and Sn are present in minor amounts (0.20(1) and 1.21(3) wt.%, respectively). The refined value of the HH unit cell parameter a = 5.93143(1) Å is in a good agreement with already published results obtained from PXD/SR-PXD (5.9300(1) Å) [13, 14] and PND (5.9298(1) Å) [11, 12] for the same system. The Bragg peaks of the main phase have a subtle shoulder on the left-hand side which can be successfully modeled by

the software asymmetry parameters. The refined occupancy of the *4d* site by Ni atoms is insignificant (zero within the ESD) and the final refined composition of this HH phase agrees well with the nominal one (Table 1). Isotropic displacement parameters, refined for each element individually (B_{iso}), are reasonably low and do not suggest any disorder in the crystal structure.

For the sample with the nominal composition of HfNiSn, the main HH phase accounts only for 92.9(6) wt.% (Figure S2, Table 1). The additional phases are FH ($HfNi_2Sn$), Ni_3Sn_2, Hf_2Ni_2Sn and metallic Hf (1.07(2), 1.38(6), 1.07(3) and 3.61(5) wt.%, respectively). This system has not been studied by high resolution SR-PXD before. The refined value of the lattice constant for HfNiSn is a = 6.08007(2) Å, which is in good agreement with published data obtained by high-resolution PND (6.0795(1) Å) [11]. The broadening of the Bragg peaks for HfNiSn is much more pronounced than for TiNiSn (Figure 2). However, it can be successfully modelled with no need to implement a second HH phase. Similar to the Ti-based phase, HfNiSn does not reveal any disorderly distributed Ni atoms at the *4d* site. The remaining crystallographic positions *4c* and *4b* are fully occupied by Ni and Sn atoms, respectively. This observation is supported by low values of B_{iso}.

Interpretation of the data collected for the Zr-Ni-Sn system is less trivial than for the ternary compositions described above. The high-resolution SR-PXD patterns show pronounced splitting of all Bragg peaks assigned to the HH phase (Figure 2 and 3a). This suggests presence of two phases crystallizing with the same cubic symmetry but with slightly different unit cell parameters, most likely due to variations in their chemical composition. This reproducible behavior was revealed only by high-resolution SR-PXD

and was not visible in the lab diffraction patterns nor in the synchrotron data collected with a lower resolution instrument (Table 1). Two HH phases, HH_1 and HH_2, account for 72.1(3) wt.% and 26.0(2) wt.%, respectively. Refined values of the lattice constant are: a_1 = 6.11259(1) Å and a_2 = 6.10695(1) Å (Figure 3a). While the first one corresponds well with the values reported for sintered ZrNiSn samples by Xie et al. [16] and Miyazaki et al. [17], for which presence of excess Ni was confirmed, the second one is in agreement with the lattice parameter published by Downie et al. [11, 14] for stoichiometric ZrNiSn. A disordered distribution of Ni atoms over both crystallographic sites is observed for HH_1 (98.4% at *4c* and 1.3% at *4d*), but there is no indication of excess Ni since the total occupancy of Ni atomic positions is 99.7(2)%. An observed enlarged unit cell volume can therefore be due to disorder Ni atoms at the *4c* and *4d* sites rather than due to excess Ni in the structure. In HH_2, a higher concentration of Ni atom vacancies at the *4c* site is observed (occupancy of 96.8(4)%). Rietveld refinements also suggest negligible presence of Ni atoms at the *4d* site (zero within the ESD value). In both HH_1 and HH_2 crystal structures an ordered distribution of Sn atoms (100%) at the *4b* site is confirmed. The displacement parameters, refined individually for each element, adapt reasonably low values for both phases. Summary of Rietveld refinements for all ternary phases are listed in Table 1.

2.1.2. Pseudo-ternary $M_{0.5}M'_{0.5}NiSn$ and $M_{0.5}M'_{0.25}M''_{0.25}NiSn$ phases

The powder diffraction pattern for the sample with the nominal composition $Hf_{0.5}Zr_{0.5}NiSn$ is successfully indexed by four phases: two HH phases that in total account for 97.5 wt.% (HH_1 = 79.0(1) wt.% and HH_2 = 18.5(1) wt.%), Zr_5Sn_4 (1.71(5) wt.%) and Sn (0.79(3) wt.%) (Figure 3b, Table 2). Hf and Zr have been reported to form a continues

solid solution within the whole composition range for $M_{1-x}M'_xNiSn$, but multiple HH phase formation in $Hf_{0.5}Zr_{0.5}NiSn$ has also been suggested [14]. Based on laboratory PXD data, Downie et al. [14] showed strong asymmetry and broadening of Bragg peaks for (Hf,Zr)NiSn but did not observe any splitting. The refined HH_1 lattice constant a_1 = 6.09540(1) Å is comparable to the reported values (6.0926(1)[11] and 6.0931(1)[11, 14], while a_2 = 6.10017(1) Å is somewhat bigger. The calculated chemical compositions, based on Vegard's law [24, 25] and assuming 1:1:1 stoichiometry, are: HH_1 – $Hf_{0.43}Zr_{0.57}NiSn$ and HH_2 – $Hf_{0.20}Zr_{0.80}NiSn$, but Rietveld refinements give the following stoichiometries: HH_1 – $Hf_{0.78}Zr_{0.22}Ni_{1.16}Sn$ and HH_2 – $Hf_{0.29}Zr_{0.71}NiSn$. The refined composition of HH_2 is rather close to the estimation from the unit cell volume, while the values obtained for HH_1 suggest formation of Hf-rich phase with a significant fraction of extra nickel that occupies disorderly the *4d* site (Figure 4a, Table 2). The observed expansion of the HH_1 unit cell volume could then be linked to the presence of additional Ni at the *4d* position rather than the Hf/Zr ratio at the *4a* site alone. Due to the high degree of correlation between refined parameters, only the overall displacement parameters were refined for each phase.

The SR-PXD data obtained for $Hf_{0.5}Ti_{0.5}NiSn$ do not differ much from the reported ones and confirm formation of multiple HH phases with various chemical compositions (Figure 2 and S3, Table 2). However, the number of HH compounds in the present sample is greater than in previously reported samples with identical nominal stoichiometry [9, 11, 14]. The diffraction pattern suggests formation of five different crystalline HH phases, a_1 = 5.93027(4) Å, a_2 = 5.95906(7), a_3 = 5.97687(8) Å, a_4 = 6.03262(4) Å, a_5 = 6.05576(9) Å, and Sn. Refinements of occupancy factors at the *4a* and *4c* atomic sites result in the following compositions: HH_1 – TiSnNi, HH_2 – $Hf_{0.10}Ti_{0.90}SnNi$, HH_3 – $Hf_{0.29}Ti_{0.71}SnNi$,

HH_4 –$Hf_{0.50}Ti_{0.50}SnNi_{0.98}$, HH_5 – $Hf_{0.60}Ti_{0.40}SnNi_{0.98}$. In HH_4 and HH_5, Ni vacancies are likely to be formed and their concentration reaches the level of 2% in both phases. Due to the complex phase composition and high number of fitting parameters, refinement of the *4d* site occupancy was not possible.

$Ti_{0.5}Zr_{0.5}NiSn$ shows similar multiphase tendency. Bragg peaks from five different HH phases and Sn can be seen in the SR-PXD pattern (Figure 2 and S4, Table 2). The refined lattice constants are: a_1 = 5.9638(1) Å, a_2 = 5.9998(2) Å, a_3 = 6.0555(1) Å, a_4 = 6.0877(1), a_5 = 6.0968(2) Å. However, for this sample the determination of the occupancy was not possible for any atomic position in the crystal structure. Thus based on these refined unit cell parameters only chemical compositions using Vegard's law were calculated under the assumption of a stoichiometric Ni and Sn content (HH_1 – $Ti_{0.82}Zr_{0.18}SnNi$, HH_2 – $Ti_{0.62}Zr_{0.38}SnNi$, HH_3 – $Ti_{0.29}Zr_{0.71}SnNi$, HH_4 – $Ti_{0.10}Zr_{0.90}SnNi$, HH_5 – $Ti_{0.06}Zr_{0.94}SnNi$). Comparison of refined and calculated stoichiometries for the (Hf,Zr)NiSn phases suggests that the latter one can be trusted only if no extra Ni is found in the empty cubic sublattice. Therefore, one could assume that values calculated for HHs in $Ti_{0.5}Zr_{0.5}NiSn$ correspond to real values only if the *4d* site is unfilled.

$Ti_{0.5}Hf_{0.25}Zr_{0.25}NiSn$ also reveals a multiphase behavior but forms only three HH phases (Figure 2, 4b and S5, Table 2). Additionally, there are traces of TiO, ZrO and Sn. The refined unit cell parameters are: a_1 = 5.97604(6) Å, a_2 = 6.04160(3) Å, a_3 = 6.07421(5). A similarity between a_1 and the unit cell parameter of TiNiSn can suggest crystallization of at least one Ti-rich phase. The obtained values are close to the numbers reported by Schwall and Balke [21] for a sample with the same nominal composition, even though our applied synthesis method was different from the one used in their study. The

phase chemical compositions, obtained by Rietveld refinements of the *4a* site occupancy only, are: HH_1 = $Ti_{0.78}Hf_{0.11}Zr_{0.11}NiSn$, HH_2 = $Ti_{0.26}Hf_{0.37}Zr_{0.37}NiSn$ and HH_3 = $Ti_{0.12}Hf_{0.44}Zr_{0.44}NiSn$. Based on Vegard's law and assuming a nominally equal atomic concentration of Zr and Hf, the compositions become: HH_1 = $Ti_{0.72}Hf_{0.14}Zr_{0.14}NiSn$ HH_2 = $Ti_{0.38}Hf_{0.31}Zr_{0.31}NiSn$, and HH_3 = $Ti_{0.24}Hf_{0.38}Zr_{0.38}NiSn$. The comparison between refined compositions and those calculated from Vegard's law are plotted in Figure 4b. Even though the occupancy of the *4d* site was not refined in HH structures, the small differences between refined and calculated values suggest that HH phases formed in $Ti_{0.5}Hf_{0.25}Zr_{0.25}NiSn$ do not accommodate any extra Ni at the normally vacant crystallographic site.

For all phases in the $Hf_{0.5}Ti_{0.5}NiSn$, $Ti_{0.5}Zr_{0.5}NiSn$ and $Ti_{0.5}Hf_{0.25}Zr_{0.25}NiSn$ samples, only overall values of the displacement parameters were refined. Summary of Rietveld refinements for the pseudo-ternary compositions are listed in Table 2.

The presented structural characterization of the ternary MNiSn systems based on high-resolution SR-PXD data clearly confirms HH phase separation in ZrNiSn for the first time. One could assume that it is a result of the applied synthesis methodology, which is known to affect formation of HH phases and their chemical compositions. On the other hand, it is highly possible that the lower resolution of powder diffraction data in previous studies obscured the presence of multiple HH phases with very similar unit cell parameters. High resolution diffraction patterns collected for TiNiSn and HfNiSn do not show obvious Bragg peaks splitting but a visual inspection of the diffraction profile lines reveals noticeable difference between the peak shapes and widths. Thus, one cannot exclude a possible presence of multiple HH phases also in these compositions, which are impossible

to be discriminated even with the superb resolution of the presented SR-PXD data. None of the investigated MNiSn samples contains excess Ni. Nonetheless, in the Zr-based HH phases a disordered distribution of Ni atoms is observed; either as a shared occupancy of both *4c* and *4d* sites or through formation of vacancies. Analysis of high-resolution diffraction patterns of the pseudo-ternary systems confirms formation of multiple HH phases in all studied samples. Although $Hf_{0.5}Zr_{0.5}NiSn$ seems to be less prone to phase separation than the other compositions, splitting of HH Bragg reflections is visible in the diffraction pattern. Besides, the identified Hf-rich phase accommodates ca. 16% of the overstoichiometric Ni at the normally vacant *4d* site. This is higher than for the reported HfNiSn, where the extra Ni concentration reaches only up to 11% [19]. Analysis of all studied pseudo-ternary systems indicates that the thermodynamic stability of formed HH phases could be strongly driven by the atomic size difference between Hf, Ti and Zr. Smaller variation in the radius of Zr and Hf atoms results in crystallization of only two HH phases, while the Ti/ZrNiSn and Hf/TiNiSn systems contain five different HH compositions.

2.2. *Electron microscopy*

2.2.1. Scanning electron microscopy (SEM) with energy dispersive X-ray spectroscopy (EDS)

Variations in chemical compositions across the powder particles were assessed by SEM-EDS (Table 3 and supplementary materials). The chemical analysis of the ternary MNiSn compounds shows a homogeneous distribution of elements in the investigated

powders and reveals a very good agreement with the compositions of the HH phases as obtained by Rietveld refinements. Values of the atomic concentration for the pseudo-ternary systems are also in agreement with the SR-PXD data analysis. For the nominal $Hf_{0.5}Zr_{0.5}NiSn$ powder, both Hf-rich and Zr-rich regions are observed, but in $Hf_{0.5}Ti_{0.5}NiSn$ and $Ti_{0.5}Zr_{0.5}NiSn$ more pronounced disparity in elements distribution and concentration is revealed. This is in accordance with the presence of multiple HH phases as confirmed by SR-PXD. The EDS results obtained for $Ti_{0.5}Hf_{0.25}Zr_{0.25}NiSn$ clearly show the formation of a Ti-rich region but also areas with an increased concentration of Hf and Zr.

2.2.2. High resolution scanning transmission electron microscopy (STEM) with energy dispersive X-ray spectroscopy (EDS)

High-resolution STEM was employed to further investigate chemical compositions of the phases formed and verify whether the local atomic arrangement is in agreement with the averaged HH crystal structures. These measurements were performed for selected powders, for which the occupancies of both Ni sites were refined from SR-PXD, i.e. TiNiSn, ZrNiSn and $Hf_{0.5}Zr_{0.5}NiSn$. HAADF-STEM images of a $[110]_{HH}$-oriented TiNiSn particle are shown in Figure 5a and 5b. At these high collection angles (99–200 mrad) the contrast generated by incoherent scattering it roughly proportional to Z^2, where Z is the atomic number. Thus, the most intense (brightest) atomic columns correspond to Sn, while Ti and Ni atoms create a lower contrast. The intensity variations between the *4c* and *4d* sites (Figure 5c) confirm an ordered arrangement of Ni over *4c* in the HH crystal structure and the vacancy of the *4d* position in agreement with the Rietveld refinements. The SR-PXD analysis of HfNiSn shows the same averaged crystal structure as TiNiSn, and thus a

similar local distribution of Ni atoms can be expected for this phase. The SR-PXD results for ZrNiSn demonstrate the crystallization of two HH compounds and specific structures of both phases. However, high resolution STEM for the two Zr-containing materials revealed a thick (5–10 nm) layer of amorphous oxide, broadly covering the HH particles (Figure 6). The formation of ZrO_2 hinders the acquisition of atomically resolved HAADF-STEM images necessary for accurate structural analysis (Figure S6). Even though, the columns of Zr and Sn atoms can be clearly seen, as bright features in the dark background, it is not possible to extract unambiguous information about the Ni distribution over the *4c* and *4d* sites in the formed HH phases.

3. Conclusions

The presented study of ternary MNiSn and pseudo-ternary $M_{0.5}M'_{0.5}NiSn$/ $M_{0.5}M'_{0.25}M''_{0.25}NiSn$ HH compounds, performed with high-resolution SR-PXD, reveal the separation of HH phases in ZrNiSn and $Hf_{0.5}Zr_{0.5}NiSn$ systems, which previously only have been reported to crystallize as single phase samples. The results do not confirm the presence of excess Ni in the ternary Zr-based HH phases. Instead they suggest a disorder distribution of stoichiometric amount of Ni atoms over *4c* and the normally vacant *4d* crystallographic positions in ZrNiSn, and formation of Ni vacancies at *4c* site in $ZrNi_{0.97}Sn$. The presence of overstoichiometric Ni has been confirmed only in the pseudo-ternary $Hf_{0.5}Zr_{0.5}NiSn$ sample. The large amount of phases present in the samples for the remaining systems with mixed Hf/Ti/Zr atomic composition hinders refinements of occupancy factors at *4a* and/or *4d* sites. The high resolution STEM for TiNiSn confirms that the local distribution of atoms in the HH phases is in agreement with the averaged HH crystal

structured obtained from powder diffraction data. However, for ZrNiSn and $Hf_{0.5}Zr_{0.5}NiSn$, the microscopy studies cannot be compared with the SR-PXD results due to the formation of the oxide layers on the particles surface, which limits the quality of acquired HAADF-STEM images. This work, along with a few other available reports, demonstrate that high-resolution SR-PXD and/or PND data are indispensable to carry out reliable analysis of structural properties of HH phases. Based on the presented SR-PXD data comparison, we encourage that published powder diffraction patterns should be provided along with a parameter that could designate a quality of their resolution. So far, this is a very rare practice for most of structural studies on HH materials and strongly limits a chance for a reliable comparison of obtained results.

Funding Sources

This work was funded by the Research Council of Norway within the THELMA (No. 228854) and TOSCA (No. 228564) projects.

Acknowledgment

The authors acknowledge the skillful assistance of the staff at Swiss-Norwegian (SNBL, BM01) and ID22 beamlines, at ESRF, Grenoble, France.

References

[1] Snyder GJ, Toberer ES. Nat Mater 2008;7:105.
[2] Tritt TM. Science 1999;283:804.
[3] Zeier WG, Zevalkink A, Gibbs ZM, Hautier G, Kanatzidis MG, Snyder GJ. Angew Chem Int Edit 2016;55:6826.
[4] Zeier WG, Schmitt J, Hautier G, Aydemir U, Gibbs ZM, Felser C, Snyder GJ. Nat Rev Mater 2016;1:1.
[5] Bos JWG, Downie RA. J Phys-Condens Mat 2014;26:1.
[6] Chen S, Ren ZF. Mater Today 2013;16:387.
[7] Xie W, Weidenkaff A, Tang X, Zhang Q, Poon J, Tritt TM. Nanomaterials-Basel 2012;2:379.
[8] Graf T, Felser C, Parkin SSP. Prog Solid State Ch 2011;39:1.
[9] Kimura Y, Chai YW. Jom-Us 2015;67:233.
[10] Kohler J, Deng SQ, Lee C, Whangbo MH. Inorg Chem 2007;46:1957.
[11] Downie RA, Barczak SA, Smith RI, Bos JWG. J Mater Chem C 2015;3:10534.
[12] Downie RA, Smith RI, MacLaren DA, Bos JWG. Chem Mater 2015;27:2449.
[13] Downie RA, MacLaren DA, Smith RI, Bos JWG. Chem Commun 2013;49:4184.
[14] Downie RA, MacLaren DA, Bos JWG. J Mater Chem A 2014;2:6107.
[15] Douglas JE, Chater PA, Brown CM, Pollock TM, Seshadri R. J Appl Phys 2014;116:1635141.
[16] Xie HH, Mi JL, Hu LP, Lock N, Chirstensen M, Fu CG, Iversen BB, Zhao XB, Zhu TJ. Crystengcomm 2012;14:4467.
[17] Miyazaki H, Nakano T, Inukai M, Soda K, Izumi Y, Muro T, Kim J, Takata M, Matsunami M, Kimura S, Nishino Y. Mater Trans 2014;55:1209.
[18] Romaka VA, Fruchart D, Hlil EK, Gladyshevskii RE, Gignoux D, Romaka VV, Kuzhel BS, Krayjvskii RV. Semiconductors+ 2010;44:293.
[19] Romaka VV, Rogl P, Romaka L, Stadnyk Y, Grytsiv A, Lakh O, Krayovskii V. Intermetallics 2013;35:45.
[20] Galazka K, Populoh S, Sagarna L, Karvonen L, Xie WJ, Beni A, Schmutz P, Hulliger J, Weidenkaff A. Phys Status Solidi A 2014;211:1259.
[21] Schwall M, Balke B. Phys Chem Chem Phys 2013;15:1868.
[22] Gurth M, Rogl G, Romaka VV, Grytsiv A, Bauer E, Rogl P. Acta Mater 2016;104:210.
[23] Rodriguez-Carvajal J. Physica B 1993;192:55.
[24] Vegard L. Z Phys 1921;5:393.
[25] Vegard L, Dale H. Z Kristallogr 1928;67:148.

Table 1. Lattice parameters (*a*), weight percentages, fractional occupancies (n), displacement factors (B_{iso}) and goodness-of-fit values (χ^2) for MNiSn HH phases obtained by Rietveld analysis of high-resolution SR-PXD data. On the bottom, total weight percentages of identified impurity phases.

M			**Ti**	**Hf**	**Zr**	
a [Å]			5.93143(1)	6.08007(2)	6.11259(1)	6.10695(1)
abundance [wt.%]			98.6(3)	92.9(6)	72.1(3)	26.0(2)
refined composition			**TiNiSn**	**HfNiSn**	**ZrNiSn**	**$ZrNi_{0.97}Sn$**
M	*4a* (0,0,0)	**n**	1.0(-)	1.0(-)	1.0(-)	1.0(-)
		B_{iso} [Å^2]	0.09(2)	0.291(7)	0.30(1)	0.24(2)
Ni_1	*4c* (¼, ¼ , ¼)	**n**	1.024(8)	1.03(2)	0.984(2)	0.968(4)
		B_{iso} [Å^2]	0.32(2)	0.37(1)	0.415(9)	0.34(2)
Ni_2	*4d* (¾, ¾, ¾)	**n**	0.02(2)	0.02(2)	0.013(2)	0.005(3)
		B_{iso} [Å^2]	-	-	0.415(9)	-
Sn	*4b* (½, ½, ½)	**n**	1.005(4)	1.01(2)	1.004(1)	1.002(2)
		B_{iso} [Å^2]	0.423(9)	0.27(1)	0.33(1)	0.23(2)
χ^2			2.02	4.00	1.73	
Impurities [wt.%]			1.40(1)	7.1(1)	1.9(3)	
			$TiNi_2Sn$	$HfNi_2Sn$	ZrO	
			Sn	Hf_2Ni_2Sn	Sn	
				Ni_3Sn_2		
				Hf		

Table 2. Lattice parameter (*a*), weight percentages, fractional occupancies (n – refined, $n_{calculated}$ – obtained from Vegard's law), displacement factors (B_{iso}) and goodness-of-fit values (χ^2) for $M_{0.5}M'_{0.5}/M_{0.5}M'_{0.25}M''_{0.25}NiSn$ HH phases obtained by Rietveld analysis of high-resolution SR-PXD data.

a [Å]	**refined composition**	**abundance** [wt.%]		**$M_{0.5}M'_{0.5}$ / $M_{0.5}M'_{0.25}M''_{0.25}$**	**Ni_1**	**Ni_2**	**Sn**	**$B_{iso\_overall}$** [Å^2]	χ^2
				4a (0,0,0)	*4c* (¼, ¼ , ¼)	*4d* (¾, ¾, ¾)	*4b* (½, ½, ½)		
$Hf_{0.5}Zr_{0.5}NiSn$									2.06
6.09540(1)	**$Hf_{0.78}Zr_{0.22}Ni_{1.16}Sn$**	79.0(1)	**n**	0.78(2)/0.22(-)	1.001(3)	0.163(9)	1.0(-)	0.562(2)	
6.10146(2)	**$Hf_{0.29}Zr_{0.71}NiSn$**	18.5(1)	**n**	0.29(8)/0.71(-)	1.09(1)	-0.04(3)	1.0(-)	0.476(8)	
$Hf_{0.5}Ti_{0.5}NiSn$									3.48
5.93027(4)	**TiNiSn**	1.1(6)	**n**	0.00(-)/1.00(2)	1.01(1)	-	1.0(-)	0.7(2)	
5.95906(7)	**$Hf_{0.10}Ti_{0.90}NiSn$**	9.5(3)	**n**	0.10(1)/0.90(-)	1.02(1)	-	1.0(-)	0.9(1)	
5.97687(8)	**$Hf_{0.29}Ti_{0.71}NiSn$**	26.1(6)	**n**	0.29(1)/0.71(-)	0.99(2)	-	1.0(-)	0.16(4)	
6.03262(4)	**$Hf_{0.51}Ti_{0.49}Ni_{0.98}Sn$**	57.0(2)	**n**	0.51(3)/0.49(-)	0.98(1)	-	1.0(-)	0.16(2)	
6.05576(9)	**$Hf_{0.60}Ti_{0.40}Ni_{0.98}Sn$**	6.3(3)	**n**	0.60(2)/0.40(-)	0.98(3)	-	1.0(-)	0.21(6)	
$Ti_{0.5}Zr_{0.5}NiSn$									2.22
5.9638(1)	**$Ti_{0.82}Zr_{0.18}NiSn$**	13.6(3)	**$n_{calculated}$**	0.82/0.18	1.0(-)	-	1.0(-)	0.97(8)	
5.9998(2)	**$Ti_{0.62}Zr_{0.38}NiSn$**	26.4(6)	**$n_{calculated}$**	0.62/0.38	1.0(-)	-	1.0(-)	0.42(6)	
6.0555(1)	**$Ti_{0.29}Zr_{0.71}NiSn$**	33.9(9)	**$n_{calculated}$**	0.29/0.71	1.0(-)	-	1.0(-)	1.08(6)	
6.0877(1)	**$Ti_{0.10}Zr_{0.90}NiSn$**	11.8(5)	**$n_{calculated}$**	0.10/0.90	1.0(-)	-	1.0(-)	0.7(1)	

6.0968(2)	**$Ti_{0.06}Zr_{0.94}NiSn$**	14.0(8)	**$n_{calculated}$**	0.06/0.94	1.0(-)	-	1.0(-)	0.8(3)	
$Ti_{0.5}Hf_{0.25}Zr_{0.25}NiSn$									1.86
5.97604(5)	**$Ti_{0.78}Hf_{0.11}Zr_{0.11}NiSn$**	36.4(3)	**n**	0.775(3)/0.113(1)/0.113(-)	1.0(-)	-	1.0(-)	1.01(2)	
6.04160(3)	**$Ti_{0.26}Hf_{0.37}Zr_{0.37}NiSn$**	57.2(5)	**n**	0.262(6)/0.369(3)/0.369(-)	1.0(-)	-	1.0(-)	0.763(6)	
6.07419(5)	**$Ti_{0.12}Hf_{0.44}Zr_{0.44}NiSn$**	4.9(2)	**n**	0.12(4)/0.44(2)/0.44(-)	1.0(-)	-	1.0(-)	0.98(4)	

Table 3. Chemical compositions of MNiSn, $M_{0.5}M'_{0.5}NiSn$ and $M_{0.5}M'_{0.25}M''_{0.25}NiSn$ HH compounds as obtained by SEM-EDS.

nominal composition	Ti [at.%]	Hf [at.%]	Zr [at.%]	Ni [at.%]	Sn [at.%]
TiNiSn_averaged	**33.9(7)**	-	-	**32.3(8)**	**34(2)**
HfNiSn_averaged	-	**32(2)**	-	**35.2(5)**	**32(1)**
ZrNiSn_averaged	-	-	**32(1)**	**33.6(7)**	**34(1)**
$Hf_{0.5}Zr_{0.5}NiSn$					
area_1	-	21.4(7)	15.8(9)	30.6(5)	32(1)
area_2		20.6(6)	10.7(6)	32.9(5)	35(1)
area_3		17.8(6)	15.7(9)	32.9(6)	34(1)
area_4		16.3(9)	17.9(6)	33.1(6)	33(1)
area_5		16.2(6)	20(1)	35.0(7)	29(1)
area_6		15.7(6)	20(1)	34.9(6)	30(1)
$Hf_{0.5}Ti_{0.5}NiSn$					
area_1	26.2(4)	6.4(4)	-	33.0(7)	34(1)
area_2	24.1(3)	9.5(6)		30.4(5)	36(1)
area_3	23.0(4)	9.8(6)		35.0(7)	32(1)
area_4	21.3(3)	13.5(8)		30.3(6)	35(1)
area_5	17.1(2)	16.9(9)		34.3(6)	32(1)
area_6	14.9(2)	19(1)		32.3(6)	34(1)
area_7	13.6(2)	15.0(8)		35.9(6)	35(1)
$Ti_{0.5}Zr_{0.5}NiSn$					
area_1	27.3(5)	-	5.6(3)	32.9(8)	34(2)
area_2	23.7(4)		10.5(4)	33.4(7)	32(1)
area_3	20.8(4)		12.3(9)	32.4(8)	34(2)
area_4	20.0(3)		15.0(6)	32.5(6)	32(1)
area_5	18.4(3)		14.5(6)	33.7(8)	33(1)
area_6	17.5(3)		16.3(6)	32.2(6)	34(1)
area_7	13.9(3)		19.5(8)	33.2(8)	33(1)
area_8	11.5(2)		20.9(8)	35.2(7)	32(1)
area_9	9.8(2)		21.8(8)	33.4(7)	35(1)
$Ti_{0.5}Hf_{0.25}Zr_{0.25}NiSn$					
area_1	22.9(3)	4.7(3)	8.6(3)	32.3(6)	31(1)
area_2	22.0(3)	5.9(4)	7.2(3)	32.3(7)	32(1)
area_3	15.6(3)	10.2(7)	8.7(4)	35.4(8)	30(1)

area_4	13.3(2)	11.5(4)	10.1(6)	33.9(6)	31(1)
area_5	11.7(2)	8.9(5)	12.4(4)	30.6(5)	36(1)
area_6	9.5(1)	11.1(6)	12.6(4)	35.5(6)	31(1)
area_7	8.4(1)	13.3(5)	12.9(8)	35.3(7)	30(1)

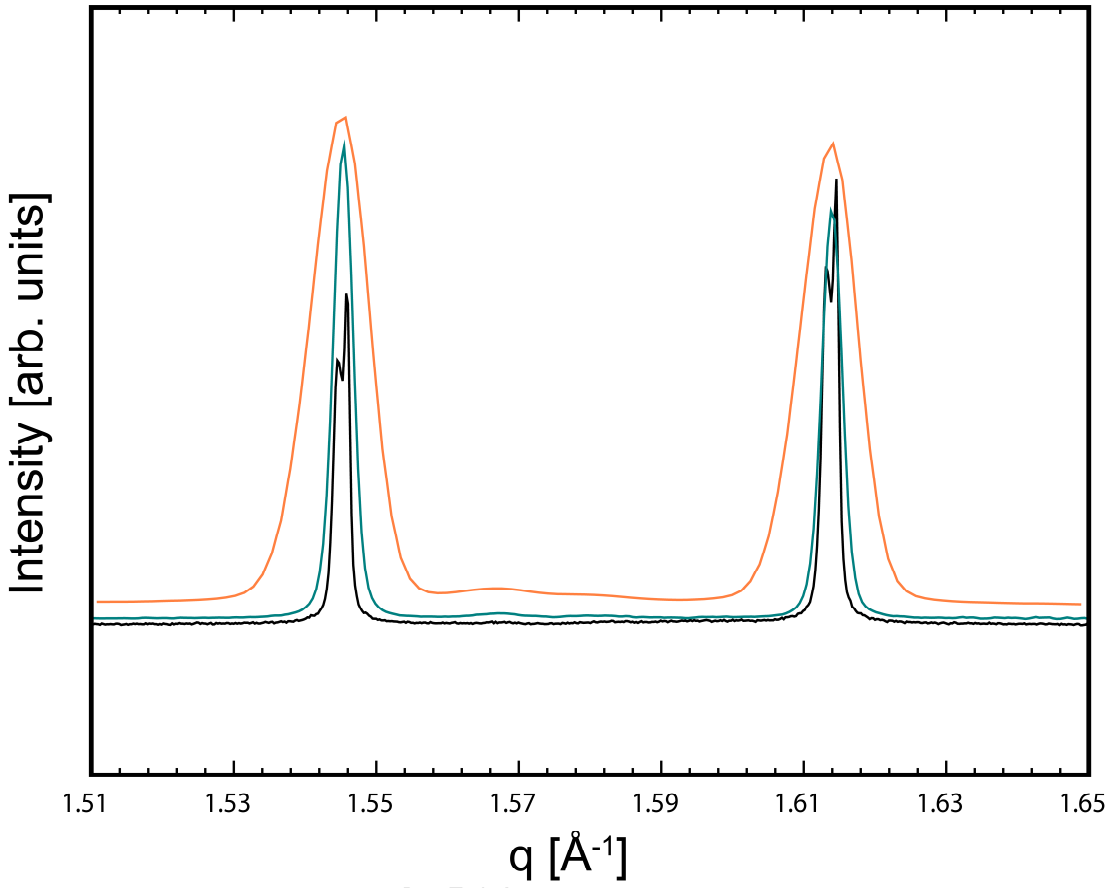

Figure 1. SR-PXD patterns collected for ZrNiSn with different instrumental setups; orange – standard resolution mode, multipurpose PILATUS@SNBL diffractometer at BM01, ESRF; green – high resolution mode, multipurpose PILATUS@SNBL diffractometer at BM01, ESRF; black – high resolution diffractometer at ID22, ESRF.

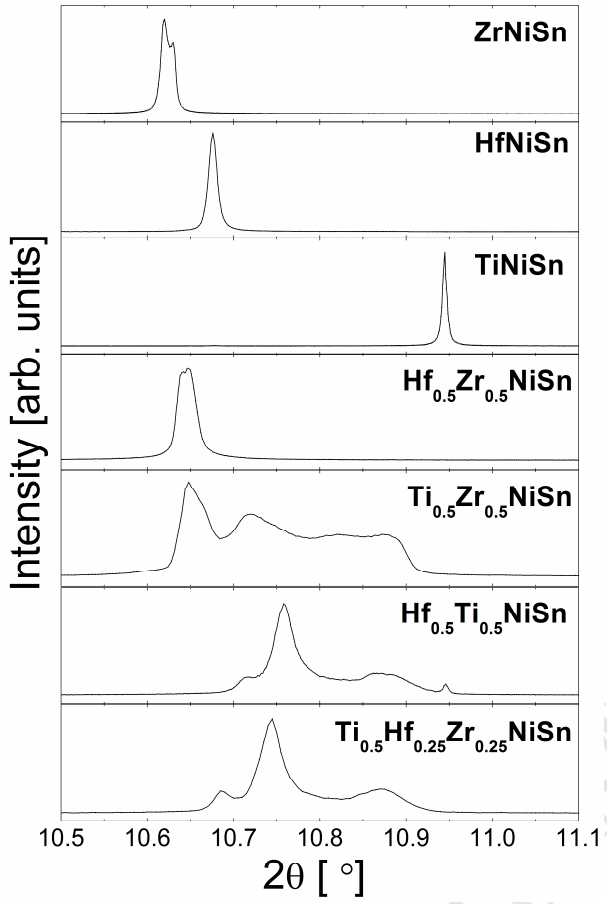

Figure 2. High resolution SR-PXD profile of (220) Bragg peak for all investigated HH systems, $\lambda = 0.4000$ Å.

a) **b)**

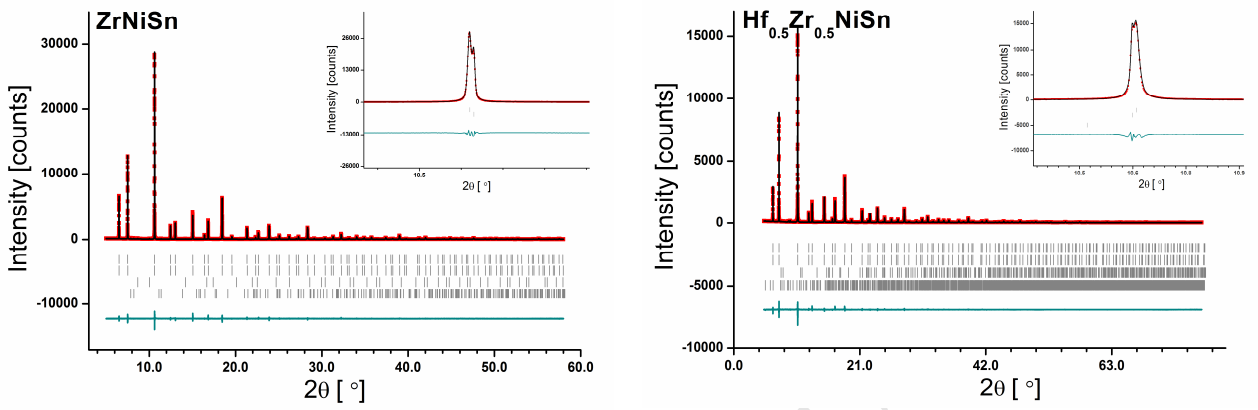

Figure 3. Observed (red), calculated (black) and difference (blue) SR-PXD profiles, λ = 0.4000 Å, for (**a**) ZrNiSn, χ^2= 1.73; and (**b**) $Hf_{0.5}Zr_{0.5}NiSn$, χ^2= 2.06. Vertical bars indicate Bragg peak positions of contributing phases, from top to bottom: (**a**) HH_1, HH_2, ZrO and Sn; (**b**) HH_1, HH_2, Sn, Zr_5Sn_4. Insets show (220) reflection.

a) **b)**

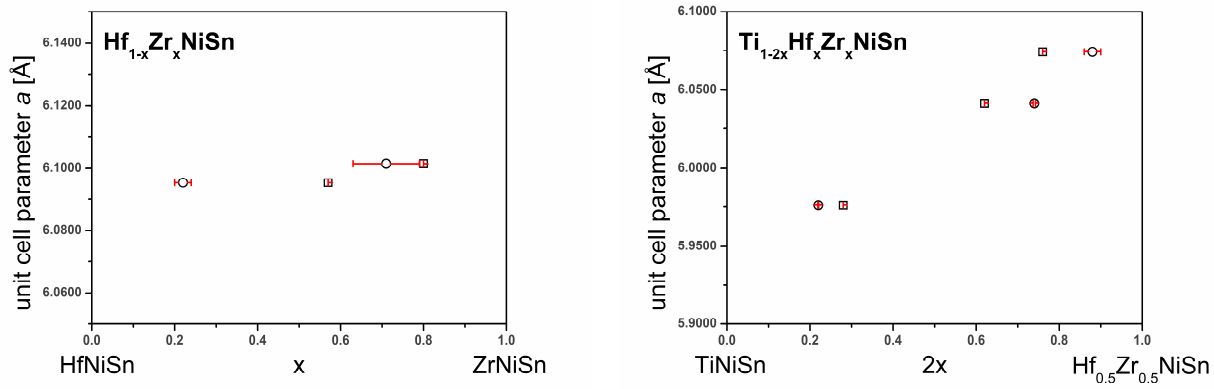

Figure 4. Refined (circles) vs. calculated from Vegard's law (square) *a* axis as a function of metal fractions (x) in HH phases formed in (**a**) $Hf_{0.5}Zr_{0.5}NiSn$ and (**b**) $Ti_{0.5}Hf_{0.25}Zr_{0.25}NiSn$. Error bars for *a* are omitted as they are smaller than the size of the symbols (Table 2).

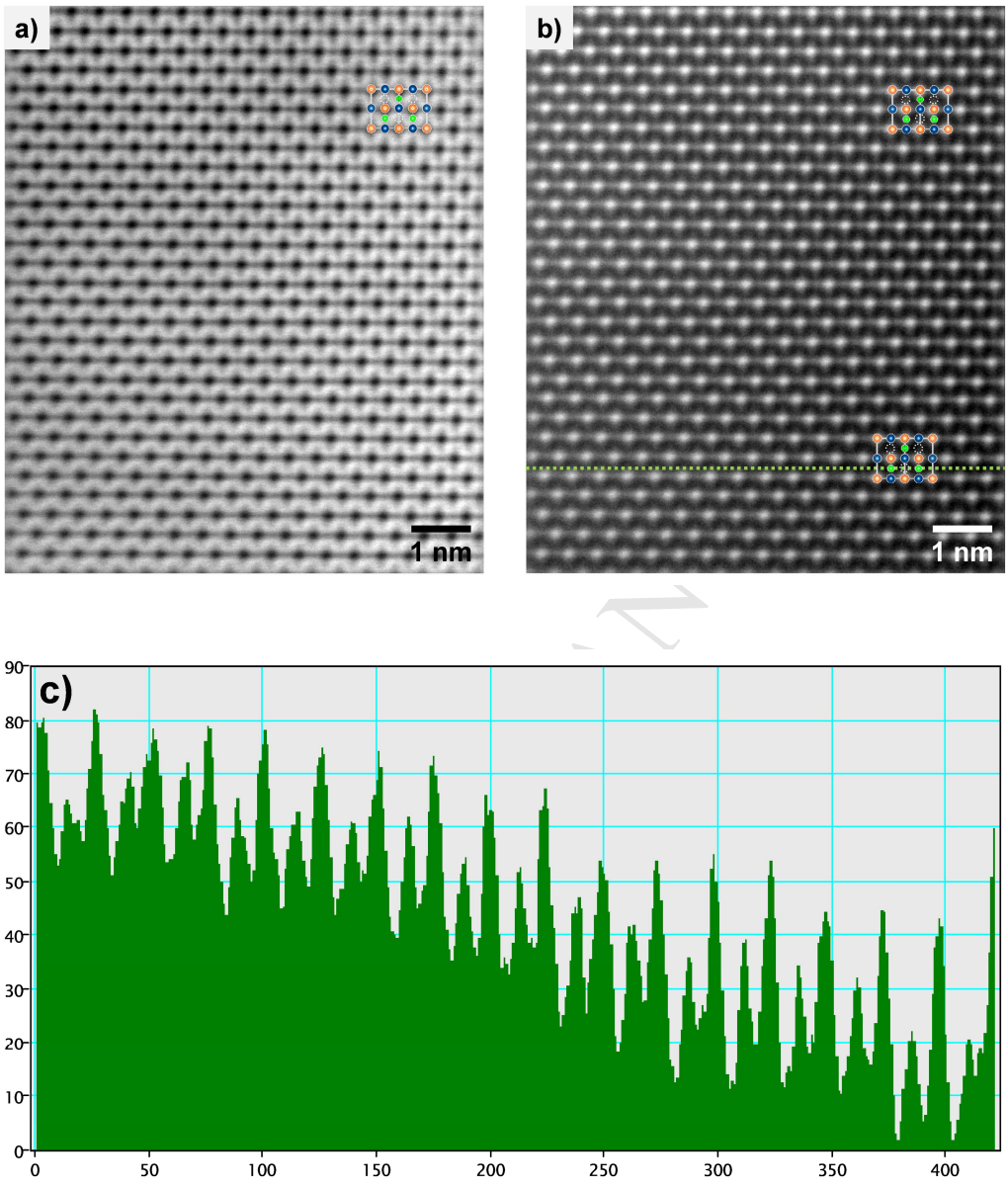

Figure 5. (**a**) ABF-STEM image of TiNiSn obtained with a convergence angle of 31 mrad and a collection angle range of 10-22 mrad; (**b**) HAADF-STEM image of the same region obtained with a convergence angle of 31 mrad and a collection angle range of 99-200mrad. The TiNiSn particle was observed along a $[110]_{HH}$ zone axis. The overlays show schematic representations of the HH unit cell (blue, orange and green circles represent Ti, Sn and Ni at *4c*, respectively;

dashed white circles indicate the vacant *4d* site); (**c**) intensity profile along sequential *4c* and *4d* sites as observed along the dashed line in (**b**) confirming the ordered distribution of Ni atoms in the HH crystal structure of TiNiSn.

a)

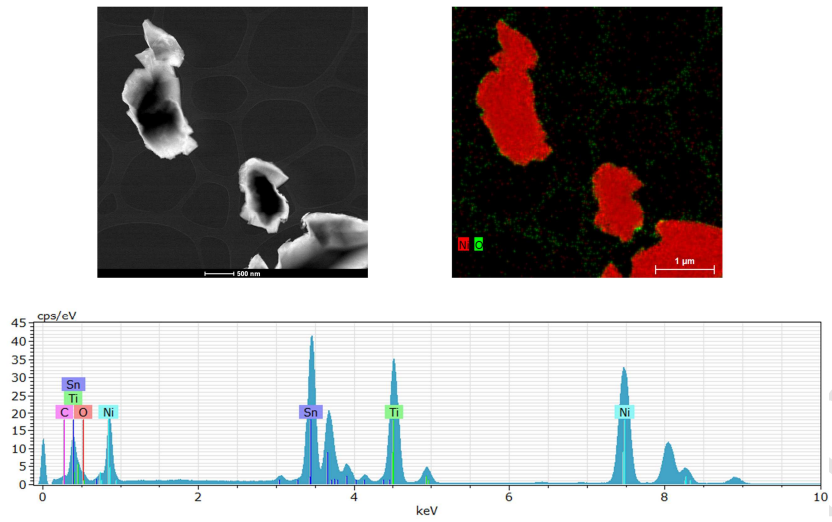

b)

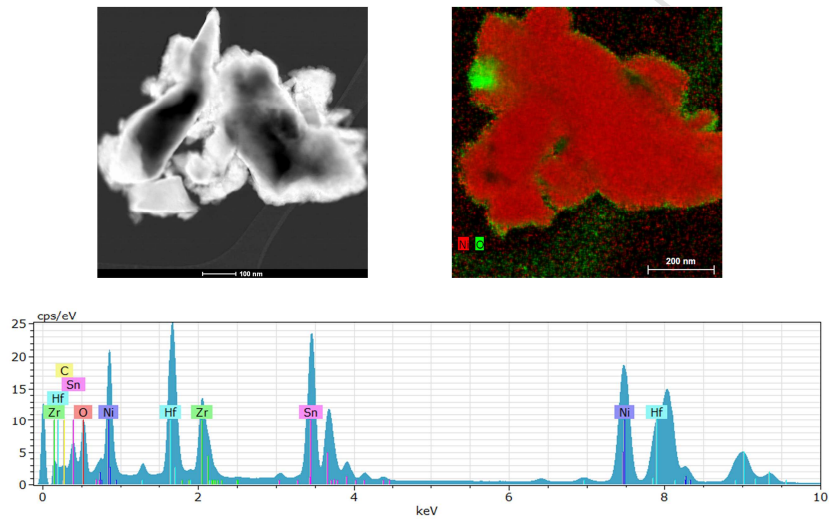

Figure 7. The low-magnification HAADF-STEM images with corresponding EDS maps and spectra for (**a**) TiNiSn and (**b**) $Hf_{0.5}Zr_{0.5}NiSn$ indicating a significant difference in presence of oxygen-rich regions (low in (**a**) and high in (**b**)) between both compositions.